Available online at www.sciencedirect.com
ScienceDirect
Trans. Nonferrous Met. Soc. China 34(2024) 1908−1921
Transactions of Nonferrous Metals Society of China
www.tnmsc.cn

Electrochemical corrosion behavior of nanostructured BCC-$Al_{0.5}CoCrFeNi_{0.4}$ high-entropy alloy in sodium chloride solution

Bo-wei ZHANG[1,2], Ze-qun ZHANG[1], Qi-juan DONG[1], Jun-sheng WU[1,2], Ning ZHUANG[1], Peng-cheng ZUO[1], Xiao-gang LI[1,2]

1. Institute for Advanced Materials and Technology, University of Science and Technology Beijing, Beijing 100083, China;
2. National Materials Corrosion and Protection Data Center, University of Science and Technology Beijing, Beijing 100083, China

Received 21 December 2022; accepted 25 June 2023

Abstract: The electrochemical corrosion behavior of $Al_{0.5}CoCrFeNi_{0.4}$ high-entropy alloy (HEA) in 3.5 wt.% NaCl solution was investigated by electrochemical measurements coupled with comprehensive characterization of its surface films. The results demonstrate that the $Al_{0.5}CoCrFeNi_{0.4}$ HEA primarily consists of (Al,Ni)-rich *B*2 phase and (Cr,Fe)-rich *A*2 phase. When subjected to electrochemical polarization, an ultrathin passive film rich in Cr is homogeneously formed on the surface. As the applied potential increases, the protective film tends to break down at the interface of two phases, followed by the preferential dissolution of *B*2 phase. Finally, the surface film with a triple-layer structure is formed on the HEA surface. Specifically, the inner layer and the middle layer are enriched in Cr and Fe, respectively, due to the high stability of Cr species and the selective dissolution of Fe. The (Al,Ni)-rich corrosion products are found to deposit at the outmost position ascribed to the dissolution of *B*2 phase.

Key words: high-entropy alloy; electrochemical corrosion behavior; selective corrosion; transpassivation; triple-layer oxide film

1 Introduction

High-entropy alloys, a sort of multi-element alloys with near equimolar proportions, have been regarded as promising structural materials ascribed to their exceptional service performances, such as combined high strength and ductility [1−3], enhanced fracture toughness [4,5] and excellent corrosion resistance [6,7]. As a typical HEA category, AlCoCrFeNi HEAs have attracted extensive attention with favorable mechanical and anti-corrosion properties [8,9]. Previous studies demonstrated that AlCoCrFeNi HEAs even exhibit superior corrosion resistance compared to 304 stainless steel in various aggressive media [10,11].

It is widely acknowledged that the corrosion behavior of the alloys is highly dependent on their microstructural features, such as the grain size [12], phase distribution [13], crystalline orientation [14], and grain boundary type [15]. According to the relative studies [16−18], phase constitution is found to be closely associated with the corrosion resistance of AlCoCrFeNi HEAs, which is mainly determined by the molar ratios of the component elements. Among the most common phases, the face-centered cubic (FCC) phase exhibits slightly superior anti-corrosion properties than the other two body-centered cubic (BCC) phases, in which the (Al,Ni)-rich *B*2 phase is likely to be preferentially

Corresponding author: Bo-wei ZHANG, Tel: +86-10-62333931, E-mail: bwzhang@ustb.edu.cn
DOI: 10.1016/S1003-6326(24)66515-5

etched in aggressive media due to its higher electrochemical activity than other phases [19,20]. According to Ref. [11], the galvanic effect between *B*2 phase and surrounding FCC phase could lead to the accelerating dissolution of the former and produce severe localized corrosion. Moreover, YEN et al [19] reported that *B*2 phase tends to be initially corroded away due to its lower charge transfer resistance and the poorer uniformity of the passive film based on the first principle calculation.

As a promising corrosion resistance alloy, AlCoCrFeNi HEAs will be inevitably applied in some harsh environments like bleaching or radiation, thus taking the high risk of transpassive dissolution [10,21,22]. Nevertheless, there has still been no study focusing on the transpassivation behavior of high-entropy alloys so far. It is well-known that the transpassivation process of stainless steels is mainly due to the dissolution of Cr as Cr(III) and Fe as Fe(III) through the transpassive film [23,24], which is also considered to be a pathway for the AlCoCrFeNi HEAs. Actually, the distinctive transpassivation behavior of these HEAs has been noticed but not further studied [25]. Compared to stainless steels, the presence of Al element and (Al,Ni)-rich *B*2 phase is believed to greatly influence their transpassive dissolution process at high anodic potentials.

In the present work, the $Al_{0.5}CoCrFeNi_{0.4}$ high-entropy alloy was fabricated and went through structural analysis and electrochemical corrosion behavior investigation by means of multiple characterization techniques. Initially, microstructural and compositional features of the HEA were analyzed by X-ray diffraction (XRD), electron back-scattered diffraction (EBSD) and energy-dispersive X-ray spectroscopy (EDX). Subsequently, the electro-chemical corrosion behavior of the HEA in 3.5 wt.% NaCl solution was evaluated by potentiodynamic polarization curves, followed by the compre-hensive transmission electron microscopy (TEM) characterization of the oxide films formed in passive and transpassive regions, respectively. Based on the results above, the electrochemical corrosion mechanism of $Al_{0.5}CoCrFeNi_{0.4}$ high-entropy alloy was proposed. The present study is beneficial to strengthening the fundamental understanding of the electrochemical corrosion behavior of multi-phase HEAs and serving as references for the corresponding corrosion control and alloy design.

2 Experimental

2.1 Materials

The non-equimolar $Al_{0.5}CoCrFeNi_{0.4}$ HEA was fabricated by arc melting using commercially pure Al, Fe, Cr, Co, and Ni particles with the purity up to 99.99% under the high-purity argon atmosphere. Melting and casting were subsequently carried out in a vacuum of 1.013×10^3 Pa followed by purging with argon three times. The alloy was repeatedly melted and solidified six times to achieve high chemical homogeneity. The chemical composition of the as-cast alloy is shown in Table 1. The specimens for electrochemical measurements were cut into 10 mm × 10 mm × 2 mm plates and sealed in epoxy resin with an exposure area of 1 cm^2. The studied surfaces of specimens were mechanically polished using a series of $400^{\#}$−$2000^{\#}$ SiC grit papers, polished with diamond suspensions, cleaned with alcohol and deionized water and dried before electrochemical measurements.

Table 1 Chemical composition of as-cast $Al_{0.5}CoCrFeNi_{0.4}$ alloys (at.%)

Al	Co	Cr	Fe	Ni
6.62	28.93	25.52	27.41	11.52

2.2 Electrochemical measurements

The potentiodynamic polarization and EIS measurements were carried out using the Autolab Pastat 302N instrument via a three-electrode electrochemical cell system, in which a saturated calomel electrode (SCE) was used as the reference electrode, a platinum foil as the counter electrode, and a specimen as the working electrode. The electrochemical measurements were undertaken in 3.5 wt.% NaCl solution at room temperature. Before the electrochemical test, the specimens were cathodically polarized at −1 V (vs REF) for 10 min to remove the air-formed oxide film on the surface. Then, the sample was immersed in the solution for 1 h to reach a stable value of the open circuit potential (OCP). The EIS tests were performed at the stable OCP with a sinusoidal potential amplitude of 10 mV and the frequency range was changed from 100 kHz to 10 mHz. The Zsimpwin software was used to analyze the EIS data. The potentiodynamic polarization curve was measured

at a scan rate of 1 mV/s from −0.5 V (vs OCP) to the final potential with a current density of 1 mA/cm^2. All experiments were repeated at least three times to confirm the reliability of data. According to relevant research [26−28], constant potential polarization measurements were carried out in 3.5 wt.% NaCl solution at −0.15 and 0.75 V for 1 h, respectively, to ensure that sufficiently stable films were formed on the samples.

2.3 Microstructure analysis

X-ray diffraction (XRD) analysis was performed at 2θ values from 20° and 90° at a scanning rate of 5 (°)/min using an X-ray equipment with Cu K_α radiation (STOE/2, 3 kW). The EBSD analysis was conducted by a Tescan mira 3 LMH scanning electron microscope equipped with an Oxford Instrument Symmetry EBSD detector. Scanning electron microscopy (SEM, Regulus 8100) was employed to observe and analyze the microstructure of the as-cast alloy. For better observation, the surface of the samples was slightly etched with a mixed solution of 30 mL glycerol + 10 mL HNO_3 + 30 mL HCl. The scanning transmission electron microscopy (STEM) images and EDX mappings were obtained by transmission electron microscope (TEM, Talos F200s). The SKPFM measurement (AFM, Bruker) was conducted to measure the appearance and potential on the surface of HEA. The contents of various elements of the HEA dissolved in 3.5 wt.% NaCl solution after constant potential polarization were evaluated by inductively coupled plasma mass spectrometry (ICP-MS). The cross-section images and EDX mappings of samples after polarization were observed through focused ion beam-SEM (FIB-SEM) using a Helios 600i SEM (FEI, USA). X-ray photoelectron spectroscopy (XPS) test was performed on a Thermo ESCALAB Model 250XI instrument to analyze the composition of the surface film.

3 Results and discussion

3.1 Microstructure

Figure 1 shows the microstructural features of the as-fabricated $Al_{0.5}CoCrFeNi_{0.4}$ HEA. The low-magnification SEM image (Fig. 1(a)) and inverse pole figure (IPF) map (Fig. 1(b)) suggest that the alloy possesses an anisotropic characteristic with an average grain size exceeding 500 μm. Upon further inspection, the magnified SEM observation exhibits

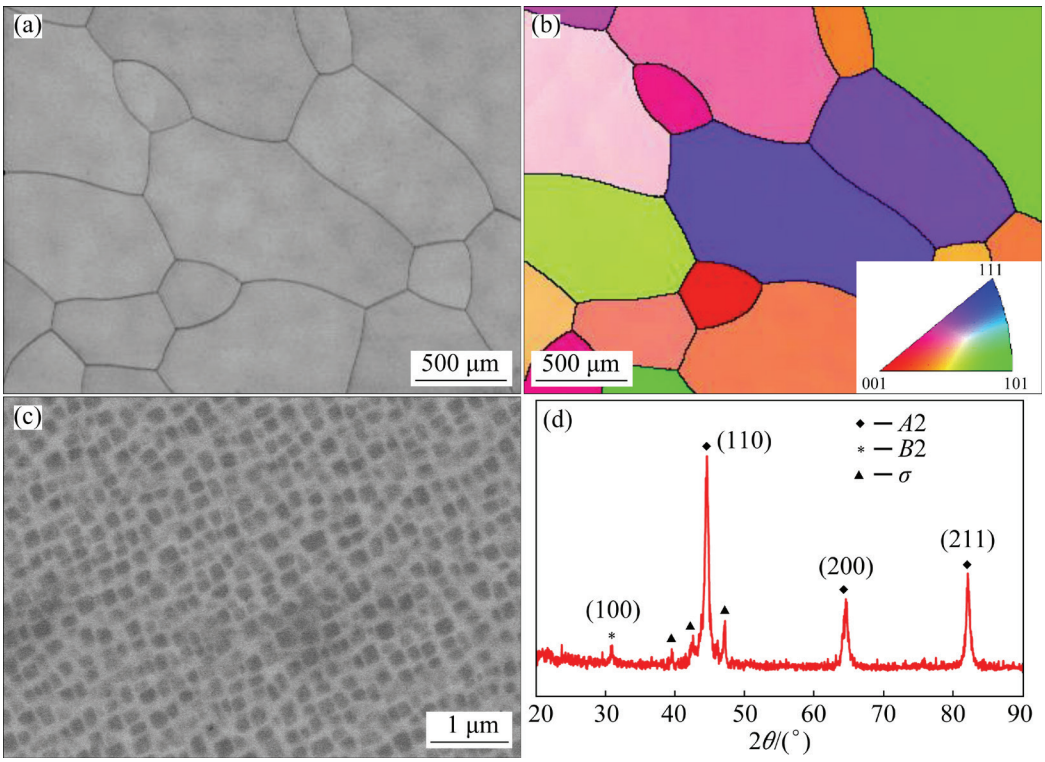

Fig. 1 Low SEM image (a), IPF map (b), high magnification BSE image (c) and XRD pattern (d) of $Al_{0.5}CoCrFeNi_{0.4}$ HEA

that the large-scale grain is composed of plentiful nano-scale grains, which can be easily distinguished from the *z*-contrast between the grains and the intergranular regions, as shown in the back-scattered electron (BSE) image of Fig. 1(c). The XRD pattern in Fig. 1(d) demonstrates that the HEA mainly consists of BCC phase (i.e. disordered *A*2 phase and ordered *B*2 phase) with trace amount of σ phase [29].

In order to further characterize the elemental distribution of the nanostructured HEA, STEM equipped with EDX was employed. As illustrated in Fig. 2(a), the size of the nano-grains is measured to be around 200 nm, which is consistent with the BSE results mentioned above. Element distribution maps in Figs. 2(c−f) clearly demonstrate the composition difference between the grains and intergranular regions. It is observed that the nano-grains are mainly composed of Al and Ni whilst the intergranular regions are rich in Fe and Cr. In contrast, Co is homogeneously distributed in both parts. According to the reported results, the (Fe,Cr)-rich regions represent the *A*2 phase and the (Al,Ni)-rich grains are the *B*2 phase [30,31]. As listed in Table 2, the total content of Al and Ni is merely ~6 at.% in *A*2 phase but it can reach almost ~50 at.% in *B*2 phase. By comparison, the molar ratios of Fe to Cr exhibit an utterly different situation. As for Co, it shows similar content in the two phases. It is well-known that the electrochemical stability of the material is highly dependent on its chemical composition. Based on the SKPFM measurement of the $Al_{0.5}CoCrFeNi_{0.4}$ HEA, the *B*2 phase possesses a much lower volta potential compared with the *A*2 phase (Fig. 2(h)), as indicated by the darker contrast in Figs. 2(g) and (h), which is attributed to the high content of Al in *B*2 phase.

3.2 Electrochemical corrosion behavior

Figure 3 shows the anodic potentiodynamic polarization curves of the $Al_{0.5}CoCrFeNi_{0.4}$ HEA in 3.5 wt.% NaCl solution, in which two plateaus are included in the low and high potential ranges, respectively. It is noted that the current density experiences a rapid boost after the first plateau, followed by a sharp decrease before reaching the second plateau. In order to understand the electrochemical process that occurred between the HEA and the electrolyte, the electrochemical impedance spectroscopy measurements were carried out at −0.15 and 0.75 V located within the two plateaus, respectively. As illustrated in Fig. 3(b), the Nyquist plots at two potentials exhibit an identical semicircle shape and the larger diameter of the semicircle indicates better corrosion resistance. Figure 3(c) shows the Bode plots of HEA after polarization at −0.15 and 0.75 V, respectively. The curves of both samples show a similar trend, but the sample polarized at −0.15 V possesses a larger value of the maximum impedance modulus. In the high frequency range, the sample possesses a constant impedance modulus and a phase angle of approximately 0°, indicating the existence of a pure resistor (the solution resistance) [32]. Moreover, in the medium and low frequency ranges, the lg $|Z|$

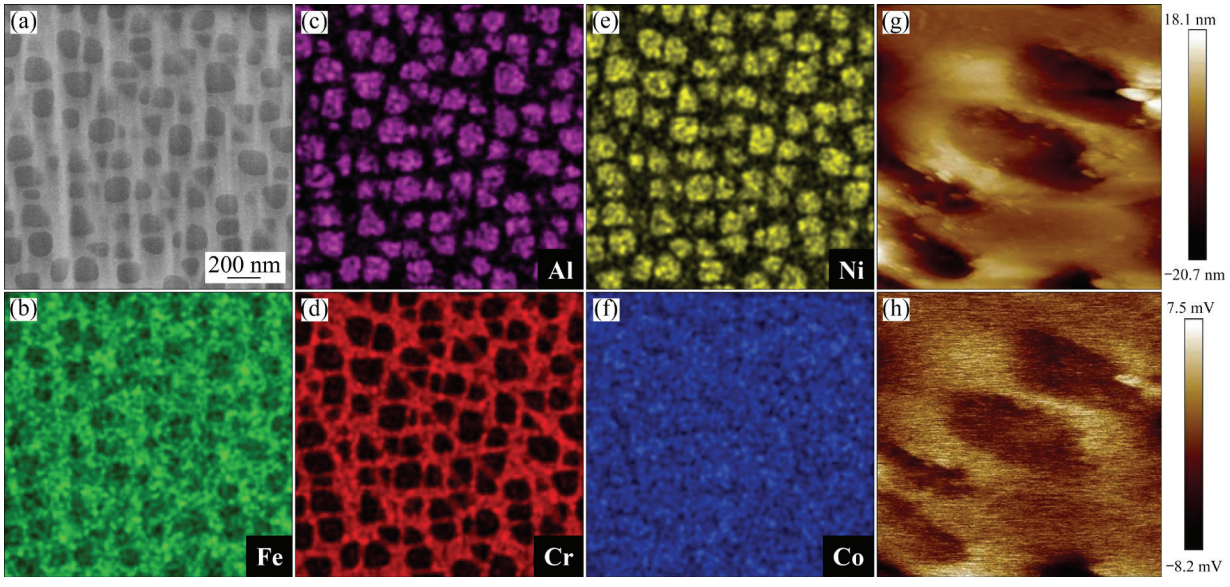

Fig. 2 STEM-EDX mappings (a−f) and SKPFM mappings (g, h) of phases in $Al_{0.5}CoCrFeNi_{0.4}$ HEA

Table 2 EDX results of two phases (*A*2 and *B*2) in $Al_{0.5}CoCrFeNi_{0.4}$ HEA (at.%)

Phase	Al	Cr	Fe	Co	Ni
*A*2	1.49	40.67	29.69	23.73	4.42
*B*2	24.20	5.68	16.60	29.42	24.10

and lg *f* show the linear relationships and the phase angles reach maximum values for both plots, which is related to the capacitive-like response of passive film [33,34]. As shown in Fig. 3(d), the electrical equivalent circuit model with two-time constants is used to fit the EIS results. In the equivalent circuit, R_s is the solution resistance, Q_1 indicates the constant phase element (CPE) related to the capacitance of the surface film, R_1 represents the resistance of surface film, Q_2 reflects the interfacial electric double-layer capacitance, and R_2 refers to the charge transfer resistance [34]. The fitting parameters are shown in Table 3. The value of R_1 for the sample polarized at −0.15 V (2.72×10^3 Ω·cm^2) is much higher than that of the sample polarized at 0.75 V (45.67 Ω·cm^2), indicating the alloy polarized at −0.15 V exhibits slightly better corrosion resistance.

Except for the electrochemical measurements, microscopic characterizations were also employed to further reveal the microstructural features of the oxide films formed on the HEA surface at the two potentials, respectively. Figure 4(a) shows the current density−time (*J*–*t*) curve of the $Al_{0.5}CoCrFeNi_{0.4}$ HEA in 3.5 wt.% NaCl solution measured at −0.15 V, suggesting that the current density undergoes an initial drop and then remains stable. Figure 4(b) illustrates the inductively coupled plasma mass spectrometry (ICP-MS) results after the *J*–*t* measurement at −0.15 V for 1 h. It can be witnessed that Al and Fe are dominant in the solution due to their higher activities compared to the other three elements, although the general dissolution rate of the HEA is low. The surface morphology of the HEA after *J*–*t* measurement was observed under SEM and TEM, respectively. The BSE image in Fig. 4(c) clearly shows the phase contrast between *A*2 and *B*2 phases, which is consistent with the alloy without constant potential polarization measurement. Since no corrosion pits or products were witnessed on the smooth surface of HEA, TEM observation with a higher resolution

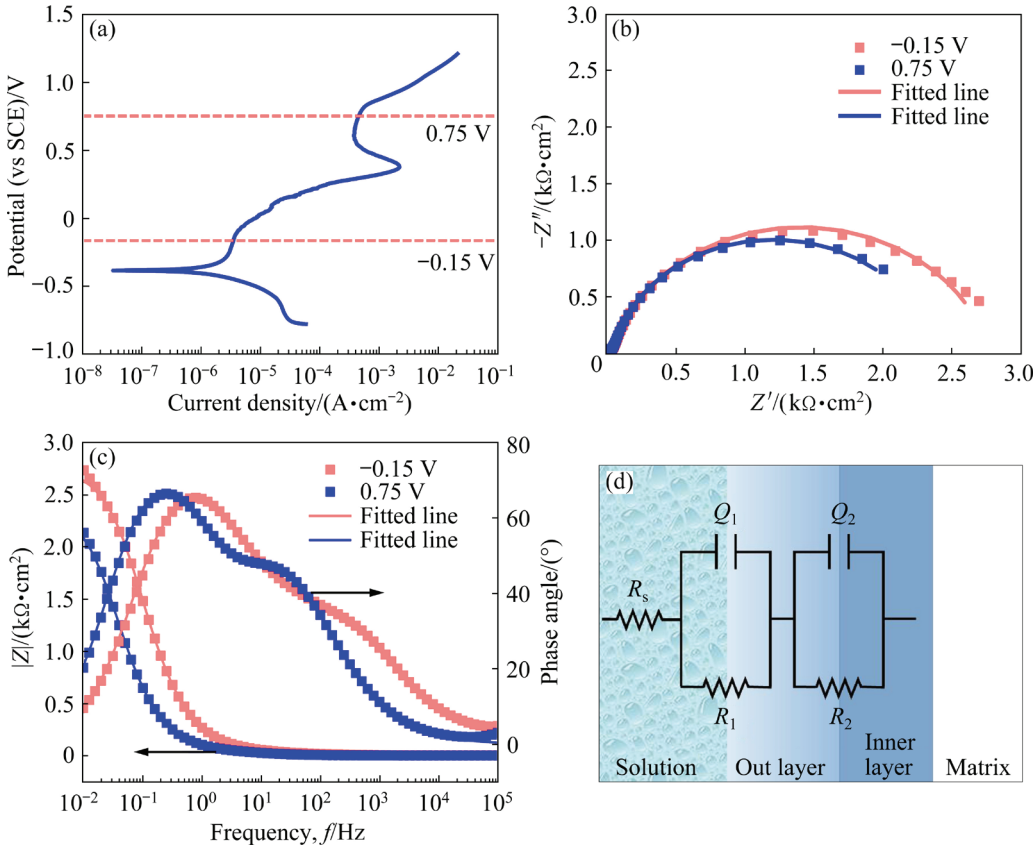

Fig. 3 Potentiodynamic polarization curve (a), Nyquist plots (b) and Bode plots (c) of HEA, and electrical equivalent circuit for fitting EIS data (d)

Table 3 Fitting parameters of EIS measurements

Potential (vs SCE)/V	R_s/ ($\Omega\cdot cm^2$)	Q_1/ ($\Omega^{-1}\cdot cm^{-2}\cdot s^n$)	n_1	R_1/ ($\Omega\cdot cm^2$)	Q_2/ ($\Omega^{-1}\cdot cm^{-2}\cdot s^n$)	n_2	R_2/ ($\Omega\cdot cm^2$)
−0.15	5.05	7.71×10^{-4}	0.87	2.72×10^{3}	1.42×10^{-5}	0.91	42.46
0.75	4.81	0.24×10^{-4}	0.69	45.67	0.02×10^{-5}	0.58	2.31×10^{3}

n, n_1 and n_2 are exponents of constant phase angle elements

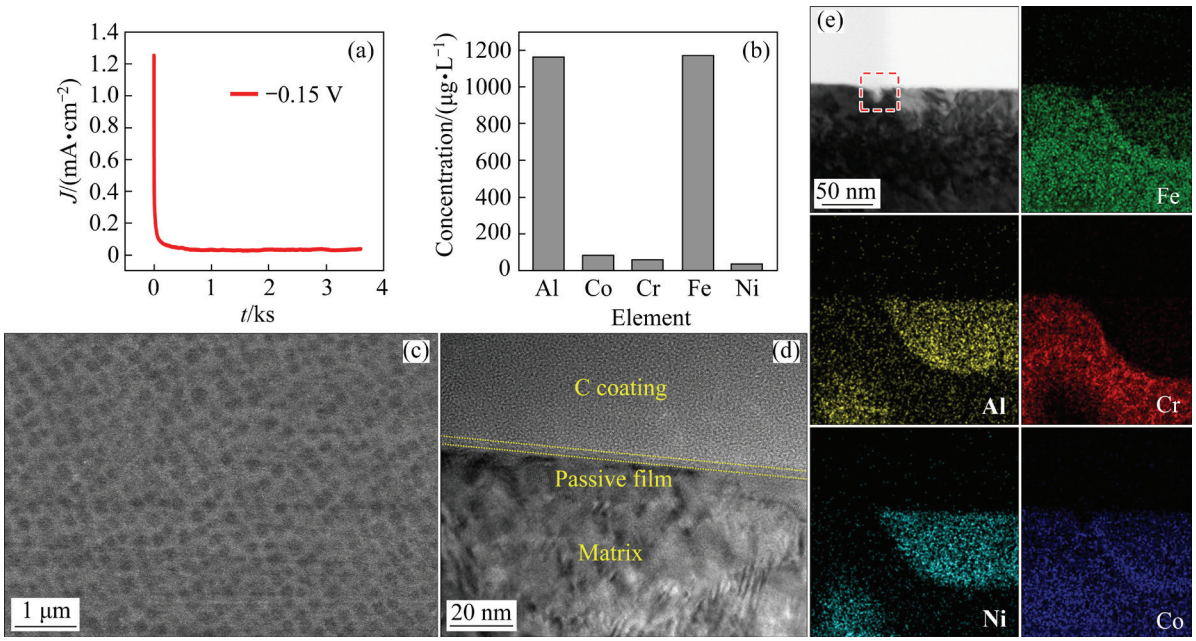

Fig. 4 Potentiostatic polarization curve of $Al_{0.5}CoCrFeNi_{0.4}$ HEA at −0.15 V (a), corresponding elemental concentrations obtained by ICP analysis (b), top and cross-section view images of HEA after polarization at −0.15 V, respectively (c, d), and EDX mappings of interface between passive film and substrate (e)

was adopted to further characterize the surface condition details of the HEA. The cross-sectional specimen of the HEA was prepared by using the focused ion beam (FIB), as displayed in Fig. 4(d). It is seen that an ultrathin passive film with a thickness of ~3 nm is formed on the surface of the HEA matrix, which could well explain the smooth surface observed in the SEM (Fig. 4(c)). A carbon coating was seen to be deposited on top of the passive film for protection during sample preparation by FIB. The magnified STEM image and the interface and elemental maps are shown in Fig. 4(e). The thin passive film could be identified from its *z*-contrast, which is much brighter than the matrix and slightly darker than the carbon coating. It is noteworthy that a tiny pit is observed to be initiated on the HEA surface. Compared with the elemental mappings, it could be inferred that the pit just locates at the grain boundary between the (Al,Ni)-rich *B*2 phase grain and (Fe,Cr)-rich *A*2 phase. This is probably ascribed to the micro-galvanic effect between the two phases as well as the slightly higher electrochemical activity of their boundary [35]. Due to the ultrathin thickness of the passive film as well as the intense signals from the HEA substrate, the composition information cannot be well reflected in the STEM maps.

In order to reveal the chemical composition of oxide film formed on the surface, XPS was used to characterize the $Al_{0.5}CoCrFeNi_{0.4}$ HEA after the polarization at −0.15 V. As shown in Fig. 5(a), the XPS survey spectrum indicates the existence of Al, Co, Cr, Fe, Ni and O elements in oxide film. Figures 5(b−f) illustrate the high-resolution XPS spectra of Al 2p, Co 2p, Cr 2p, Fe 2p and Ni 2p, respectively. It is seen that all detailed spectra of HEA exhibit two main spin-orbit peaks, $2p_{3/2}$ and $2p_{1/2}$, which are separated by analogous binding energies [36]. In detail, the Al 2p spectrum can be fitted into three peaks at the binding energies of 72.1, 73.3 and 74.3 eV, corresponding to metallic Al $2p_{3/2}$, Al $2p_{1/2}$, Al_2O_3 and $Al(OH)_3$ (Al^{3+}),

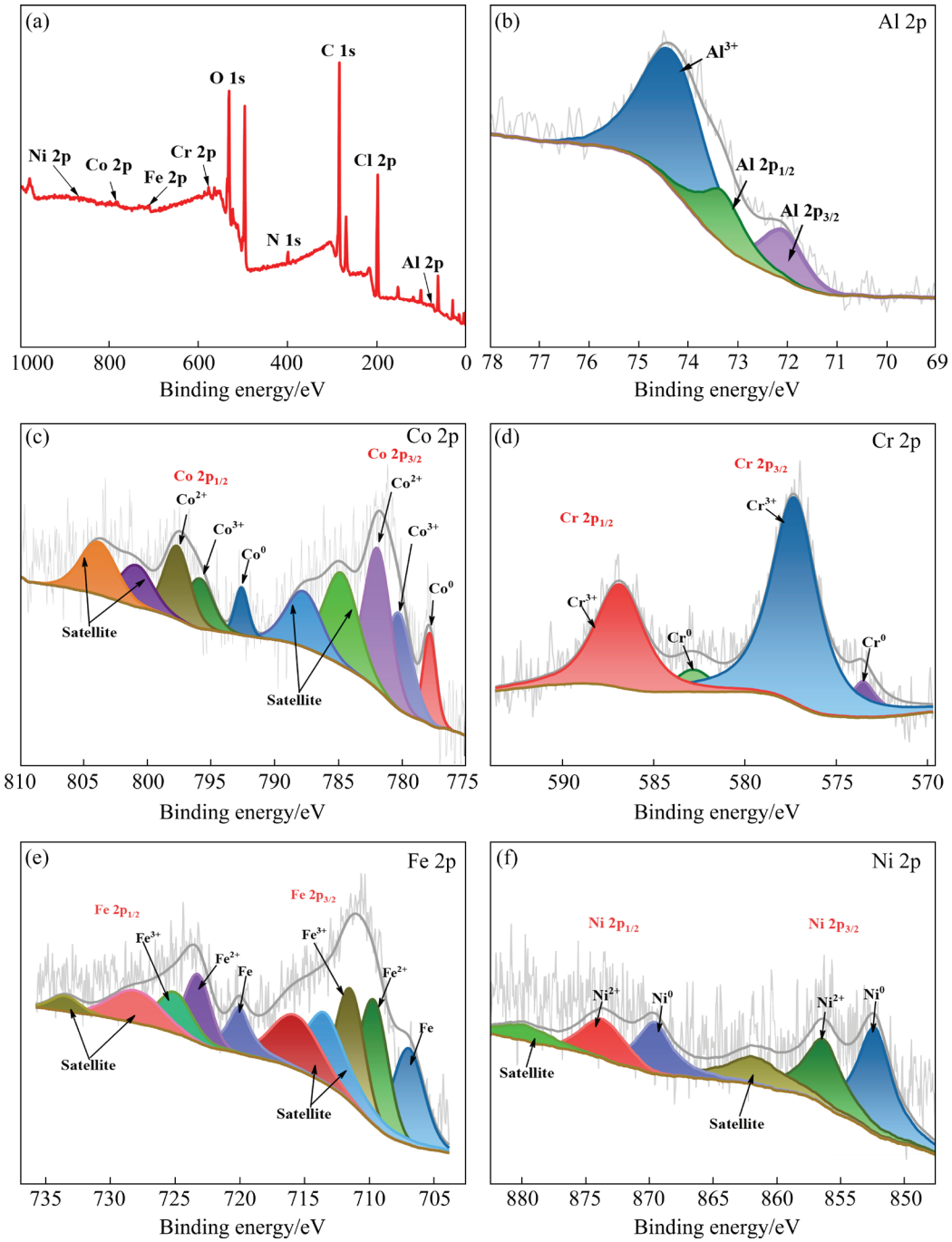

Fig. 5 XPS spectra of sample polarized at −0.15 V: (a) Survey of all elements; (b−f) High-resolution spectra of Al, Co, Cr, Fe and Ni, respectively

respectively [28,32,36]. The Co, Co^{3+} and Co^{2+} peaks with binding energies of 777.8, 780.2 and 781.9 eV can be observed in the high-resolution XPS spectrum of Co $2p_{3/2}$, which may indicate the presence of metallic Co, CoO, $Co(OH)_2$ and Co_3O_4, respectively [34,37]. It can be seen in Fig. 5(d) that the Cr $2p_{3/2}$ peak is separated into the peaks of the Cr_2O_3 and $Cr(OH)_3$ (Cr^{3+}) at 577.2 eV and a weak peak of metallic Cr at 573.9 eV [34]. Similar to Co $2p_{3/2}$, Fe $2p_{3/2}$ spectrum mainly contains three constituent peaks, including metallic Fe (706.9 eV), Fe^{2+} (709.6 eV) and Fe^{3+} (711.5 eV), which can be attributed to the presence of FeO, Fe_2O_3 and FeOOH in the film, respectively [21,26,27]. The Ni $2p_{3/2}$ peak can be deconvoluted into three components at the binding energies of 852.9, 855.7 and 860.9 eV, which are assigned to metallic Ni, NiO and $Ni(OH)_2$ (Ni^{2+}), and Ni_{sat}, respectively [37].

The fitting results of spin-orbit $2p_{1/2}$ peaks of each element show similar results with the $2p_{3/2}$ peaks above. As such, the main composition of the passive film formed on the surface of the $Al_{0.5}CoCrFeNi_{0.4}$ HEA is a mixture of the metallic oxides/hydroxides of each constituent element.

The electrochemical corrosion behavior of the HEA was further investigated at an applied potential of 0.75 V at the second plateau. The corresponding *J*–*t* profile is shown in Fig. 6(a). Similar to the previous case, the current density rapidly reached a flat level, indicating the stabilization of the HEA surface at such a high potential. As shown in the ICP results (Fig. 6(b)), the content of Ni in the solution after being polarized at 0.75 V is significantly higher than that of other elements, which is closely associated with a large amount of dissolution of the Ni-rich *B*2 phase. Figure 6(c) exhibits the surface morphology of the HEA after being subjected to the potentiostatic polarization above. Combined with Fig. 2, it can be observed that serious corrosion occurred on the surface of HEA. A large number of *B*2 phase nano-grains have dissolved and plentiful corrosion pits are left on the substrate, which is consistent with the cross-section STEM image in Figs. 6(d) and (e). It is seen that a porous oxide film (~ 60 nm) is homogeneously covered on the surface of HEA and the quasi-cubic *B*2 grains are completely etched away. According to the magnified view and EDX mappings in Fig. 6(e), the surface film can be further divided into three layers, in which O and Co are homogeneously distributed. The strong enrichment of Cr is identified at the film/metal interface as the inner layer. The layer with Fe enrichment (middle layer) could be detected on the Cr-rich layer, where other elements are deficient, attributing to the passive film initially formed on the surface of HEA. This bilayer structure is identical to that of stainless steel, which is due to the preferential dissolution caused by the different oxide formation potentials of Cr and Fe and the high diffusion rate of Fe in passive film [38−43]. Similar to the mechanism above, once the HEA sample is immersed in the solution, the Cr element is preferentially oxidized while other constituents gradually dissolve at low rates, leaving Cr enriched in the film within a short time [44,45]. In general, the stable Cr species enriched in the passive film could effectively isolate the contact between corrosive medium and substrate to improve corrosion resistance [34]. The enrichment of Fe in the middle layer can be ascribed to the selective dissolution of Fe to generate oxides/hydroxides species on the surface [40,45]. After being polarized at 0.75 V, severe corrosion and the massive dissolution of Fe from matrix lead to the formation of a relatively thick layer. After the protective film is destroyed, corrosion of the alloy occurs and the (Al,Ni)-rich *B*2 phase dissolves

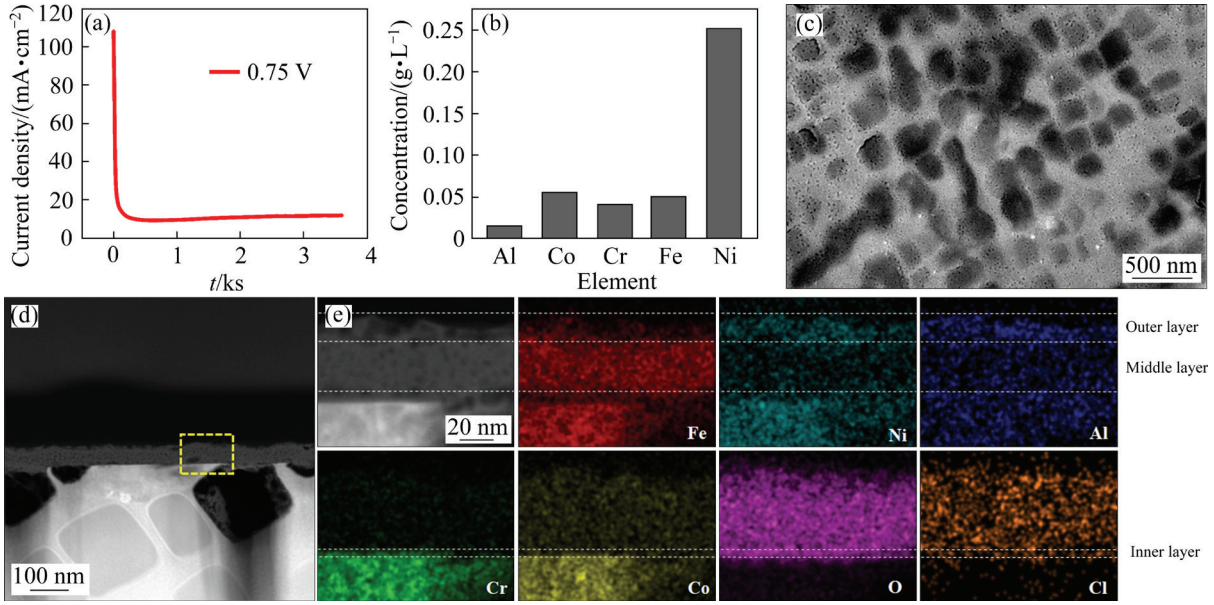

Fig. 6 Potentiostatic polarization curve of $Al_{0.5}CoCrFeNi_{0.4}$ HEA at 0.75 V (a), corresponding elemental concentrations obtained by ICP analysis (b), top and cross-section view images of HEA after polarization at 0.75 V, respectively (c, d), and EDX mappings of interface between surface film and substrate (e)

into the corrosive environment [46], which is in agreement with the high content of Ni in the solution after polarization (Fig. 6(b)). Al and Ni oxide species redeposited in solution cover the Fe-rich film as the outer layer with the abundance of Al and Ni, as illustrated by the mapping results. Different from the dense inner passive film, the middle and outer layers of surface film exhibit porous structures, which is due to the enrichment of iron oxides/hydroxides and the original porous structure of aluminum oxides/hydroxides [28,37,47, 48]. In order to further explore the specific compositions of the film formed on the surface of HEA after polarization at 0.75 V, XPS measurements were also employed.

Figure 7 shows the survey spectra and high-resolution spectra of Al, Co, Cr, Fe and Ni of the HEA after being polarized at 0.75 V. The Al, Co, Cr, Fe, Ni and O elements are detected in the oxide film formed on the surface of HEA. Similar to Fig. 5, two main spin-orbit peaks ($2p_{3/2}$ and $2p_{1/2}$) are also identified in every detailed spectrum. The Al 2p spectrum is separated into three constituent peaks at the binding energies of 71.9, 72.3 and 74.3 eV,

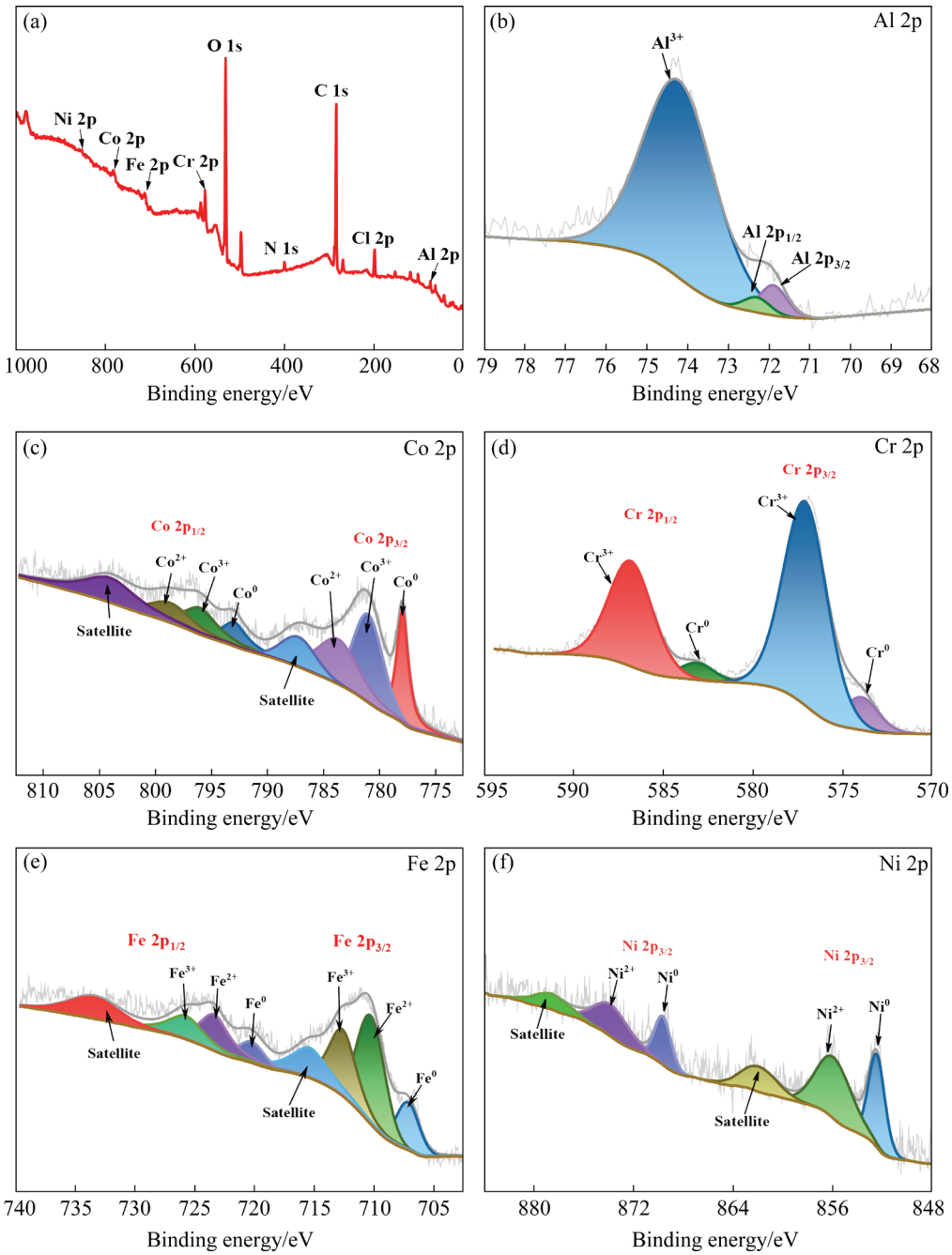

Fig. 7 XPS spectra of sample polarized at 0.75 V: (a) Survey of all elements; (b−f) High-resolution spectra of Al, Co, Cr, Fe and Ni, respectively

representing Al $2p_{3/2}$, Al $2p_{1/2}$, Al_2O_3 and $Al(OH)_3$ (Al^{3+}), respectively [28,32,36]. The Co $2p_{3/2}$ spectrum contains three decomposed peaks corresponding to Co (777.9 eV), Co^{3+} (781.0 eV) and Co^{2+} (783.7 eV), which illustrates the presence of metallic Co, CoO, $Co(OH)_2$ and Co_3O_4 in film [34,37]. As shown in Cr $2p_{3/2}$ spectrum, the deconvoluted peaks at the binding energies of 574.0 and 577.2 eV indicate the existence of metallic Cr, Cr_2O_3 and $Cr(OH)_3$ (Cr^{3+}), respectively [34]. The peaks located at 707.2, 710.3 and 712.6 eV in Fe 2p spectrum are assigned to Fe, Fe^{2+} and Fe^{3+}, representing the mixture of metallic Fe and ferric compounds (including FeO, Fe_2O_3 and FeOOH) [21,26,27]. The spectrum of Ni $2p_{3/2}$ could be well-fitted with components at 852.5 eV corresponding to the metal (Ni) and at 856.3 eV associated with NiO and $Ni(OH)_2$ (Ni^{2+}) [37]. It is similar in the composition of the two surface films formed after polarization at different potentials by comparing Figs. 5 and 7. Combining with Fig. 6, it can be concluded that the main components in the inner, middle and outer layers of the surface film are Cr, Fe and Al−Ni oxides/hydroxides, respectively.

Based on the results above, it can be seen that the morphology and composition of the surface film change with the shift of applied potential. According to the XPS results, the contents of cationic and metallic species of Al, Co, Cr, Fe and Ni elements in the surface film are shown in Fig. 8. Overall, the contents of different elements in the film formed on the sample after polarization at −0.15 V are 41.47 at.% for Al, 7.87 at.% for Co, 27.7 at.% for Cr, 18.65 at.% for Fe and 4.31 at.% for Ni, and the contents of Al, Co, Cr, Fe and Ni elements in film on the sample after polarization at 0.75 V account for 30.23 at.%, 18.96 at.%, 24.81 at.%, 23.46 at.% and 2.55 at.%, respectively. All constituent elements of HEA are detected in both films in the form of oxides/hydroxides and metals, and the number of cations is higher than respective metallic species. In detail, the amount of metallic species decreases after being polarized at higher potential due to the formation of the surface film with bigger thickness. The high oxidation resistance of Ni results in the low content of Ni in the surface film and its large proportion of metallic form [26]. When subjected to serious dissolution of Al−Ni phase, a large amount of Ni remains in the solution and the Ni content is still low in surface

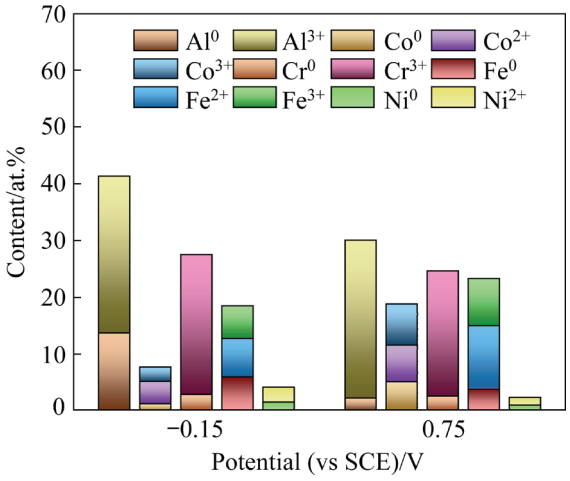

Fig. 8 Cationic content in surface films of HEA at different potentials based on XPS analysis

film. After being polarized at 0.75 V, the content of Al decreases to a certain extent, while the content of Co experiences a slight increase, which can be attributed to the selective dissolution of *B*2 phase and deposition of corrosion products. As for Cr and Fe elements, there are minor fluctuations observed in the content after different potential polarizations due to the limited corrosion of the (Cr,Fe)-rich phase. Considering the fact that the composition and structure of different layers in the surface film are determined by the enriched elements, the effect of various elements on the surface film deserves further discussion. As reported in the previous research [34,49,50], the compact chromium oxides/hydroxides could effectively improve the stability and protection of the surface films, while the aluminum oxides/hydroxides easily form surface film with porous structures and Fe species show lower stability in comparison with Cr substances. After being polarized at 0.75 V, the Cr-rich inner film with the protective effect on the surface has been broken and the porous Fe-rich middle and Al-rich outer layers cannot effectively prevent the invasion of corrosion media, resulting in the inferior corrosion resistance even though a thicker film (compared with the film on the sample polarized at −0.15 V) is formed on the surface.

3.3 Corrosion mechanism

Figure 9 exhibits the electrochemical corrosion behavior and surface film formation processes of $Al_{0.5}CoCrFeNi_{0.4}$ HEA in 3.5 wt.% NaCl solution. It

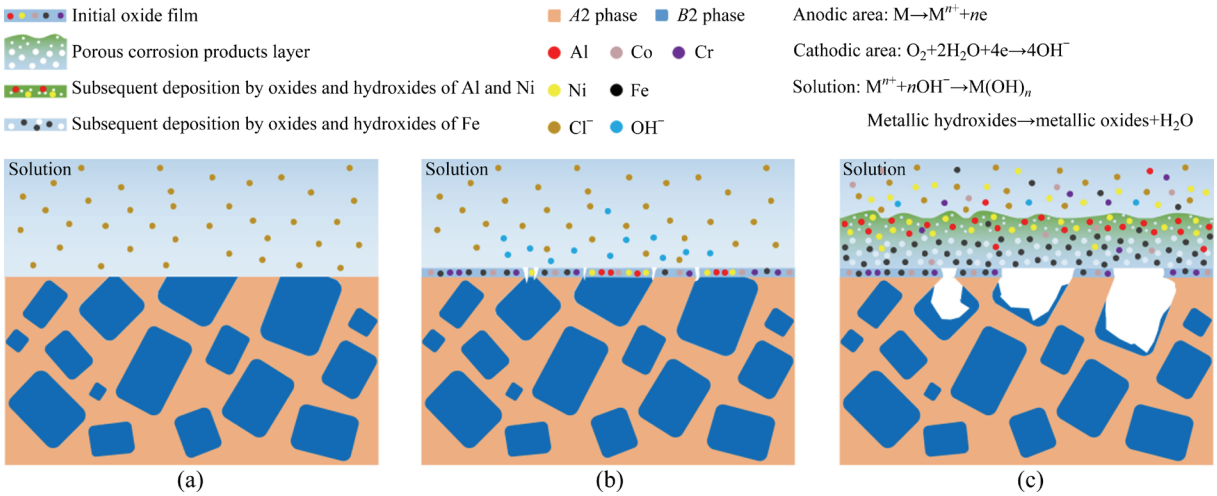

Fig. 9 Schematic diagrams showing electrochemical corrosion and surface film formation processes of $Al_{0.5}CoCrFeNi_{0.4}$ HEA in 3.5 wt.% NaCl solution: (a) Priginal state of HEA without corrosion; (b) Initial period of corrosion; (c) Period of corrosion development

is generally accepted that the composition and structure of the surface film show significant influence on the corrosion resistance of metallic alloys [26]. The complex composition of the HEA results in a mixture of multiple oxides/hydroxides species in the surface film. At the early stage of the corrosion process, the ultrathin and continuous passive film mainly consisting of Al, Cr, and Fe oxides/hydroxides is formed on the surface. The surface of Cr-rich (*A*2) phase exhibits slightly better corrosion resistant performance since a higher Cr content in the local region contributes to the stability and protectiveness of the film, while the films formed on the Al-rich (*B*2) phase are more susceptible to attack by Cl^- [28]. Driven by the galvanic effect, the breakdown of the passive film initiates at the interface between *A*2 and *B*2 phases, followed by the localized corrosion. With further development of corrosion, the weak *B*2 phase continues to rapidly dissolve, thus leading to the formation of plenty of corrosion pits. During this period, the HEA has undergone severe corrosion and the surface film is mainly composed of oxides/hydroxides generated on the surface of HEA, which can be divided into three layers: the Cr-rich inner layer, the Fe-rich middle layer and the (Al,Ni)-rich outer layer. The enrichment of Cr in the inner layer is due to the preferential oxidation of Cr and high stability of the Cr oxides. The accumulation of Fe in the middle layer is related to the selective dissolution of Fe oxides with poorer stability and higher diffusion rate in the film [51]. The deposition of corrosion products of etched *B*2 phase gives rise to the formation of (Al,Ni)-rich outer film layer. The corrosion product layers formed subsequently possess a porous structure, and the thickness is significantly larger than that of the initial thin film.

4 Conclusions

(1) The $Al_{0.5}CoCrFeNi_{0.4}$ HEA exhibits a single BCC structure, which is mainly composed of disordered *A*2 phase and ordered *B*2 phase. The *B*2 phase in the form of nano-scale grains is (Al,Ni)-rich and the *A*2 phase existed in the intergranular regions is rich in Cr and Fe, while Co is homogeneously distributed in the alloy.

(2) The initially formed ultrathin passive film tends to breakdown at the interface of *A*2 phase and *B*2 phase due to their chemical composition and stability differences. The anodic *B*2 phase would be etched with the increase of applied potential.

(3) The oxide film formed after transpassive dissolution shows a triple-layer structure, i.e. a Cr-rich inner layer, a Fe-rich middle layer and an (Al,Ni)-rich outer layer. The porous outer layer is formed due to the re-deposition of oxide/hydroxide species that are generated from dissolved *B*2 phase.

CRediT authorship contribution statement

Bo-wei ZHANG: Conceptualization, Data curation, Writing − Original draft preparation, Formal analysis; **Ze-qun ZHANG** and **Qi-juan DONG:** Data curation, Formal analysis, Simulation; **Jun-sheng WU:** Writing −

Reviewing and editing; **Ning ZHUANG** and **Peng-cheng ZUO:** Project administration, Validation; **Xiao-gang LI:** Supervision.

Declaration of competing interest

The authors declare that they have no known competing financial interests or personal relationships that could have appeared to influence the work reported in this paper.

Data availability

The data that has been used is confidential. The raw/processed data required to reproduce these findings cannot be shared at this time as this data also forms part of an ongoing study.

Acknowledgments

This work was supported by the National Natural Science Foundation of China (No. 51901018), the Young Elite Scientists Sponsorship Program by China Association for Science and Technology (Nos. YESS, 2019QNRC001), the Fundamental Research Funds for the Central Universities, China (Nos. FRF-AT-20-07, 06500119), the Natural Science Foundation of Beijing Municipality, China (No. 2212037), and the National Science and Technology Resources Investigation Program of China (No. 2019FY101400).

References

[1] YE Y F, WANG Q, LU J, LIU C T, YANG Y. High-entropy alloy: Challenges and prospects [J]. Materials Today, 2016, 19: 349−362.

[2] MIRACLE D B, SENKOV O N. A critical review of high entropy alloys and related concepts [J]. Acta Materialia, 2017, 122: 448−511.

[3] TIAN Yu-sheng, ZHOU Wen-zhe, TAN Qing-biao, WU Ming-xu, QIAO Shen, ZHU Guo-liang, DONG An-ping, SHU Da, SUN Bao-de. A review of refractory high-entropy alloys [J]. Transactions of Nonferrous Metals Society of China, 2022, 32: 3487−3515.

[4] SATHIYAMOORTHI P, KIM H S. High-entropy alloys with heterogeneous microstructure: Processing and mechanical properties [J]. Progress in Materials Science, 2022, 123: 100709.

[5] GEORGE E P, CURTIN W A, TASAN C C. High entropy alloys: A focused review of mechanical properties and deformation mechanisms [J]. Acta Materialia, 2020, 188: 435−474.

[6] FU Yu, LI Jun, LUO Hong, DU Cui-wei, LI Xiao-gang. Recent advances on environmental corrosion behavior and mechanism of high-entropy alloys [J]. Journal of Materials Science & Technology, 2021, 80: 217−233.

[7] QIU Y, THOMAS S, GIBSON M A, FRASER H L, BIRBILIS N. Corrosion of high entropy alloys [J]. NPJ Materials Degradation, 2017, 1: 15.

[8] ZHANG Xiao, LIU Liang, YAO Kun-da, DUAN Kai, WU Fu-fa, ZHAO Rong-da, ZHANG Yue, SHANG Jian, CHEN Ming-hua. The phase composition characteristics of AlCoCrFeNi high entropy alloy heat-treated by simple normalizing treatment and its effects on mechanical properties [J]. Journal of Alloys and Compounds, 2022, 926: 166896.

[9] SHI Y Z, YANG B, XIE X, BRECHTL J, DAHMEN K A, LIAW P K. Corrosion of $Al_xCoCrFeNi$ high-entropy alloys: Al-content and potential scan-rate dependent pitting behavior [J]. Corrosion Science, 2017, 119: 33−45.

[10] ALANEME K K, BODUNRIN M O, OKE S R. Processing, alloy composition and phase transition effect on the mechanical and corrosion properties of high entropy alloys: a review [J]. Journal of Materials Research and Technology, 2016, 5: 384−393.

[11] KAO Y, LEE T, CHEN S, CHANG Y. Electrochemical passive properties of $Al_xCoCrFeNi$ (x=0, 0.25, 0.50, 1.00) alloys in sulfuric acids [J]. Corrosion Science, 2010, 52: 1026−1034.

[12] RALSTON K D, BIRBILIS N. Effect of grain size on corrosion: A review [J]. Corrosion, 2010, 66: 075005.

[13] ZHAO Qian-cheng, PAN Zhi-min, WANG Xue-fei, LUO Hong, LIU Yang, LI Xiao-gang, Corrosion and passive behavior of $Al_xCrFeNi_{3-x}$ (x=0.6, 0.8, 1.0) eutectic high entropy alloys in chloride environment [J]. Corrosion Science, 2022, 208: 110666.

[14] TRISNANTO S R, WANG X L, BROCHU M, OMANOVIC S. Effects of crystallographic orientation on the corrosion behavior of stainless steel 316L manufactured by laser powder bed fusion [J]. Corrosion Science, 2022, 196: 110009.

[15] ZHANG Rui-feng, QIU Yao, QI Yuan-shen, BIRBILIS N. A closer inspection of a grain boundary immune to intergranular corrosion in a sensitised Al−Mg alloy [J]. Corrosion Science, 2018, 133: 1−5.

[16] TSAI M H, YEH J W. High-entropy alloys: A critical review [J]. Materials Research Letters, 2014, 2: 107−123.

[17] YAN Xiao-lei, GUO Hui, YANG Wei, PANG Shu-jie, WANG Qing, LIU Ying, LIAW P K, ZHANG Tao. $Al_{0.3}Cr_xFeCoNi$ high-entropy alloys with high corrosion resistance and good mechanical properties [J]. Journal of Alloys and Compounds, 2021, 860: 158436.

[18] PARAKH A, VAIDYA M, KUMAR N, CHETTY R, MURTY B S. Effect of crystal structure and grain size on corrosion properties of AlCoCrFeNi high entropy alloy [J]. Journal of Alloys and Compounds, 2021, 863: 158056.

[19] YEN C C, LU H, TSAI M, WU B W, LO Y, WANG C, CHANG S Y, YEN S K. Corrosion mechanism of annealed equiatomic AlCoCrFeNi tri-phase high-entropy alloy in 0.5 mol/L H_2SO_4 aerated aqueous solution [J]. Corrosion Science, 2019, 157: 462−471.

[20] SHI Yun-zhu, MO Jing-ke, ZHANG Feng-yuan, YANG Bin, LIAW P K, ZHAO Ying. In-situ visualization of corrosion behavior of $Al_xCoCrFeNi$ high-entropy alloys during

electrochemical polarization [J]. Journal of Alloys and Compounds, 2020, 844: 156014.

[21] DAI Chun-duo, LUO Hong, LI Jun, DU Cui-wei, LIU Zhi-yong, YAO Ji-zheng. X-ray photoelectron spectroscopy and electrochemical investigation of the passive behavior of high-entropy $FeCoCrNiMo_x$ alloys in sulfuric acid [J]. Applied Surface Science, 2020, 499: 143903.

[22] ZHANG Xian-man, CHEN Zai-yu, LUO Hong-feng, ZHOU Teng, ZHAO Yu-liang, LING Zi-cheng. Corrosion resistances of metallic materials in environments containing chloride ions: A review [J]. Transactions of Nonferrous Metals Society of China, 2022, 32: 377−410.

[23] MAURICE V, PENG H, KLEIN L H, SEYEUX A, ZANNA S, MARCUS P. Effects of molybdenum on the composition and nanoscale morphology of passivated austenitic stainless steel surfaces [J]. Faraday Discussions, 2015, 180: 151−170.

[24] UEMURA M, YAMAMOTO T, FUSHIMI K, AOKI Y, SHIMIZU K, HABAZAKI H. Depth profile analysis of thin passive films on stainless steel by glow discharge optical emission spectroscopy [J]. Corrosion Science, 2009, 51: 1554−1559.

[25] SHI Z J, WANG Z B, WANG X D, ZHANG S, ZHENG Y G. Effect of thermally induced *B*2 phase on the corrosion behavior of an $Al_{0.3}CoCrFeNi$ high entropy alloy [J]. Journal of Alloys and Compounds, 2022, 903: 163886.

[26] SUN Yi-pu, LAN Ai-dong, ZHANG Min, YANG Hui-jun, QIAO Jun-wei. Influence of lanthanum on passivity behavior of CrMnFeNi high entropy alloys [J]. Materials Chemistry and Physics, 2021, 265: 124509.

[27] DAI Chun-duo, ZHAO Tian-liang, DU Cui-wei, LIU Zhi-yong, ZHANG Da-wei. Effect of molybdenum content on the microstructure and corrosion behavior of $FeCoCrNiMo_x$ high-entropy alloys [J]. Journal of Materials Science & Technology, 2020, 46: 64−73.

[28] SHI Yun-zhu, COLLINS L, BALKE N, LIAW P K, YANG Bin. In-situ electrochemical-AFM study of localized corrosion of $Al_xCoCrFeNi$ high-entropy alloys in chloride solution [J]. Applied Surface Science, 2018, 439: 533−544.

[29] MUNITZ A, SALHOV S, HAYUN S, FRAGE N. Heat treatment impacts the micro-structure and mechanical properties of AlCoCrFeNi high entropy alloy [J]. Journal of Alloys and Compounds, 2016, 683: 221−230.

[30] AIZENSHTEIN M, HAYUN S. Synthesis of *A*2 and *B*2 phases in $Al_xCoCrFeNi$ multi-component system [J]. Metallography, Microstructure, and Analysis, 2020, 9: 305−311.

[31] KANG M J, LIM K R, WON J W, NA Y S. Effect of Co content on the mechanical properties of *A*2 and *B*2 phases in $AlCo_xCrFeNi$ high-entropy alloys [J]. Journal of Alloys and Compounds, 2018, 769: 808−812.

[32] FU Yu, DAI Chun-duo, LUO Hong, LI Dong-yue, DU Cui-wei, LI Xioa-gang. The corrosion behavior and film properties of Al-containing high-entropy alloys in acidic solutions [J]. Applied Surface Science, 2021, 560: 149854.

[33] RAY M, SINGH V B. Effect of sulfuric acid on corrosion and passivation of 316 SS in organic solution [J]. Journal of the Electrochemical Society, 2011, 158: 359.

[34] WANG Zhu, ZHANG Guo-hui, FAN Xue-hua, JIN Jie, ZHANG Lei, DU Yan-xia. Corrosion behavior and surface characterization of an equiatomic CoCrFeMoNi high-entropy alloy under various pH conditions [J]. Journal of Alloys and Compounds, 2022, 900: 163432.

[35] XIANG C, ZHANG Z M, FU H M, HAN E H, ZHANG H F, WANG J Q. Microstructure and corrosion behavior of $AlCoCrFeNiSi_{0.1}$ high-entropy alloy [J]. Intermetallics, 2019, 114: 106599.

[36] MUANGTONG P, RODCHANAROWAN A, CHAY-SUWAN D, CHANLEK N, GOODALL R. The corrosion behaviour of CoCrFeNi−x (x = Cu, Al, Sn) high entropy alloy systems in chloride solution [J]. Corrosion Science, 2020, 172: 108740.

[37] NASCIMENTO C B, DONATUS U, RÍOS C T, ANTUNES R A. Passive film composition and stability of CoCrFeNi and CoCrFeNiAl high entropy alloys in chloride solution [J]. Materials Chemistry and Physics, 2021, 267: 124582.

[38] LI Tian-shu, LIU Li, ZHANG Bin, LI Ying, WANG Xiao-lan, WANG Fu-hui. Direct observation of thin membrane passive film over the growing pit on sputtered nanocrystalline austenitic stainless steel film [J]. Electrochemistry Communications, 2015, 52: 80−84.

[39] FENG Zhi-chao, CHENG Xue-qun, DONG Chao-fang, XU Lin, LI Xiao-gang. Passivity of 316L stainless steel in borate buffer solution studied by Mott−Schottky analysis, atomic absorption spectrometry and X-ray photoelectron spectroscopy [J]. Corrosion Science, 2010, 52: 3646−3653.

[40] WANG L T, MERCIER D, ZANNA S, SEYEUX A, LAURENT-BROCQ M, PERRIÈRE L, GUILLOT I, MARCUS P. Study of the surface oxides and corrosion behaviour of an equiatomic CoCrFeMnNi high entropy alloy by XPS and ToF-SIMS [J]. Corrosion Science, 2020, 167: 108507.

[41] KOCIJAN A, DONIK Č, JENKO M. Electrochemical and XPS studies of the passive film formed on stainless steels in borate buffer and chloride solutions [J]. Corrosion Science, 2007, 49: 2083−2098.

[42] GUI Y, ZHENG Z J, GAO Y. The bi-layer structure and the higher compactness of a passive film on nanocrystalline 304 stainless steel [J]. Thin Solid Films, 2016, 599: 64−71.

[43] YANG Guang-ming, DU Ya-fei, CHEN Si-yao, REN Yong-sheng, MA Yu-long. Effect of secondary passivation on corrosion behavior and semiconducting properties of passive film of 2205 duplex stainless steel [J]. Journal of Materials Research and Technology, 2021, 15: 6828−6840.

[44] MAN Cheng, DONG Chao-fang, CUI Zhong-yu, XIAO Kui, YU Qiang, LI Xiao-gang. A comparative study of primary and secondary passive films formed on AM355 stainless steel in 0.1 mol/L NaOH [J]. Applied Surface Science, 2018, 42: 763−773.

[45] LUO Hong, LI Zhi-ming, MINGERS A M, RAABE D. Corrosion behavior of an equiatomic CoCrFeMnNi high-entropy alloy compared with 304 stainless steel in sulfuric acid solution [J]. Corrosion Science, 2018, 134: 131−139.

[46] DONG Qi-juan, JIA Wen-chao, ZHANG Ze-qun, ZHANG Ding-xin, WU Jun-sheng, ZHANG Bo-wei. Effects of Ni content on the corrosion behavior of $Al0.5CoCrFeNi_x$ high entropy alloys in acid and alkaline media [J]. Materials and Corrosion, 2022, 73: 1274−1285.

[47] ZHONG Xian-kang, LU Wun-jun, YANG Huai-jun, LIU

Min, ZHANG Yang, LIU Hong-wei, HU Jun-ying, ZHANG Zhi, ZENG De-zhi. Oxygen corrosion of N80 steel under laboratory conditions simulating high pressure air injection: Analysis of corrosion products [J]. Journal of Petroleum Science and Engineering, 2019, 172: 162−170.

[48] CHEN Long-jun, DONG Bao-jun, LIU Wei, WU Fei, LI Hai, ZHANG Tian-yi. Failure analysis of corrosion products formed during CO_2 pre-corrosion of X70 and 3Cr steels: Effect of oxygen contamination [J]. Engineering Failure Analysis, 2022, 140: 106529.

[49] SHI Yun-zhu, YANG Bin, RACK P D, GUO Shi-feng, LIAW P K, ZHAO Ying. High-throughput synthesis and corrosion behavior of sputter-deposited nanocrystalline $Al_x(CoCrFeNi)_{100-x}$ combinatorial high-entropy alloys [J]. Materials & Design, 2020, 195: 109018.

[50] NASCIMENTO C B, DONATUS U, RÍOS C T, ANTUNES R A. Electronic properties of the passive films formed on CoCrFeNi and CoCrFeNiAl high entropy alloys in sodium chloride solution [J]. Journal of Materials Research and Technology, 2020, 9: 13879−13892.

[51] WANG Zhu, JIN Jie, ZHANG Guo-hui, FAN Xue-hua, ZHANG Lei. Effect of temperature on the passive film structure and corrosion performance of CoCrFeMoNi high-entropy alloy [J]. Corrosion Science, 2022, 208: 110661.

纳米结构 BCC-$Al_{0.5}CoCrFeNi_{0.4}$ 高熵合金在氯化钠溶液中的电化学腐蚀行为

张博威[1,2]，张泽群[1]，董其娟[1]，吴俊升[1,2]，庄 宁[1]，左鹏程[1]，李晓刚[1,2]

1. 北京科技大学 新材料技术研究院，北京 100083；
2. 北京科技大学 国家材料腐蚀与防护科学数据中心，北京 100083

摘 要：采用电化学测试并结合对合金表面膜的细致表征，研究 $Al_{0.5}CoCrFeNi_{0.4}$ 高熵合金(HEA)在 3.5% NaCl (质量分数)溶液中的电化学腐蚀行为。结果表明，$Al_{0.5}CoCrFeNi_{0.4}$ HEA 主要由富含 Al、Ni 的 *B*2 相和富含 Cr、Fe 的 *A*2 相组成。在电化学极化作用下，合金表面均匀地形成了一层富含 Cr 的超薄钝化膜。随着外加电位的增加，保护膜在两相界面处破裂，随后 *B*2 相优先溶解。最后，在 HEA 表面形成三层结构的表面膜：内层富集 Cr、中间层富集 Fe，外层富集 Al 和 Ni。内层和中间层的形成可归因于 Cr 物种的高稳定性和 Fe 的选择性溶解，而腐蚀产物的沉积形成表面膜外层归因于 *B*2 相的溶解。

关键词：高熵合金；电化学腐蚀行为；选择性腐蚀；过钝化；三层结构氧化膜

(Edited by Wei-ping CHEN)